Enantiodetection of Chiral Molecules via Two-Dimensional Spectroscopy

Mao-Rui Cai[1,2] Chong Ye[3] Hui Dong,[2,*] and Yong Li[4,1,5,†]

[1]*Beijing Computational Science Research Center, Beijing 100193, China*
[2]*Graduate School of China Academy of Engineering Physics, No. 10 Xibeiwang East Road, Haidian District, Beijing 100193, China*
[3]*Beijing Key Laboratory of Nanophotonics and Ultrafine Optoelectronic Systems School of Physics,*
Beijing Institute of Technology, Beijing 100081, China
[4]*Center for Theoretical Physics and School of Science, Hainan University, Haikou 570228, China*
[5]*Synergetic Innovation Center for Quantum Effects and Applications, Hunan Normal University, Changsha 410081, China*

Enantiodetection of chiral molecules is important to chemical reaction control and biological function designs. Traditional optical methods of enantiodetection rely on the weak magnetic-dipole or electric-quadrupole interactions, and in turn suffer from the weak signal and low sensitivity. We propose a new optical enantiodetection method to determine the enantiomeric excess via two-dimensional (2D) spectroscopy of the chiral mixture driven by three electromagnetic fields. The quantities of left- and right-handed chiral molecules are reflected by the intensities of different peaks on the 2D spectrum, separated by the chirality-dependent frequency shifts resulting from the relative strong electric-dipole interactions between the chiral molecules and the driving fields. Thus, the enantiomeric excess can be determined via the intensity ratio of the peaks for the two enantiomers.

Introduction.—Chiral molecules contain two species (often dubbed as enantiomers), e.g., left-handed and right-handed chiral molecules, that are mirror images of each other but cannot be superposed on through rotations, translations, or any other combinations of these two changes [1,2]. Enantiomers share almost the same physical properties, yet have disparate chemical and biological properties [1], which lead to constant interest in investigating enantioseparation [3–5], enantioconversion [6–11], as well as enantiodetection [12–15]. The function of a drug with chiral mixture depends critically on the enantiomeric excess, characterizing the amount difference of the enantiomers. Accurately determining the enantiomeric excess, i.e., enantiodetection, is thus of critical importance, yet remains a challenging task. In the traditional enantiodetection methods including circular dichroism [13], vibrational circular dichroism [13,14], and Raman optical activity [15], the signal is typically weak since they depend on the weak magnetic-dipole or electric-quadrupole interactions.

In contrast to these traditional magnetic-dipole (or electric-quadrupole) dependent methods [13–15], some innovative approaches relying on the strong electric-dipole coupling [16–24] have been proposed in current studies of chiral molecules. These approaches adopted a cyclic three-level structure [25–27], constructed with three electromagnetic driving fields (nearly) resonantly coupled to the three related electric-dipole transitions of chiral molecules. The overall phases of the three Rabi frequencies for the two enantiomers differ by π [26,27], resulting in chirality-dependent effective Hamiltonian and thus chirality-dependent process. Such a

structure offers a feasible and universal mechanism for enantiodetection [16–23] (as well as enantiospecific state transfer [24,27–32] and enantioseparation [33–35]). However, many electric-dipole-transition–based enantiodetection methods typically require enantiopure samples as reference [17–20], limiting their applications since acquiring a standard enantiopure sample is challenging [3–11,33–35] for many molecules.

In this Letter, we propose a new method of enantiodetection via the 2D spectroscopy [36–40] in a four-level structure of gas-phase chiral molecules consisting of an upper cyclic three-level subsystem and an auxiliary level [22–24]. The three-level subsystem is formed by applying three electromagnetic driving fields, and is chirality dependent due to the π phase difference of the two enantiomers. The electric-dipole transition between the auxiliary level (e.g., ground state) and one of the upper three levels (e.g., the first-excited state) is coupled with three delayed laser pulses, producing a chirality-dependent signal for the 2D spectroscopy via the four-wave-mixing process. In our scheme, the signal is detected in time domain as a function of three time coordinates (τ, T, and t) and Fourier transformed with respect to τ and t [39,40]. The signals from the two enantiomers are mapped onto the separate peaks on the spectrum with the frequency separation depending on the applied driving fields. The relation between the peak intensities and the enantiomer quantities allows us to determine the enantiomeric excess.

Model.—The current method utilizes the generic four-level structure universally existing in gas-phase chiral
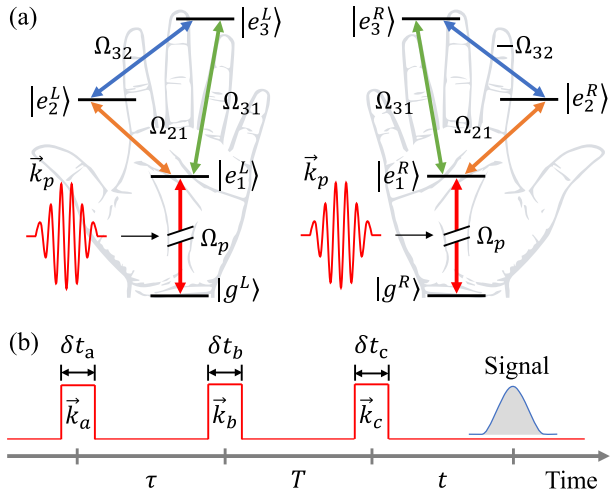
FIG. 1. The model and the pulse sequence. (a) In the cyclic three-level subsystem, three electric-dipole transitions are resonantly coupled to three electromagnetic driving fields with Rabi frequencies Ω_{21}, Ω_{31}, and $\pm\Omega_{32}$. The incident probe pulses with wave vectors $\vec{k}_p (p = a, b, c)$ are applied to induce the transition between $|g^\alpha\rangle$ and $|e_1^\alpha\rangle$ with Rabi frequencies Ω_p. (b) The squares denote the incident probe pulses under the square pulse approximation, while the curve denotes the signal.

molecules [22–24]. The structure is illustrated in Fig. 1(a), composed of a ground state $|g^\alpha\rangle$ and an upper cyclic three-level subsystem with three excited states $|e_1^\alpha\rangle$, $|e_2^\alpha\rangle$, and $|e_3^\alpha\rangle$. The index $\alpha (= L$ or $R)$ denotes the left-handed (L) or right-handed (R) chiral molecules. Three electromagnetic driving fields (e.g., microwave fields), shown in Fig. 1(a) as blue, orange, and green arrows, are constantly applied to the sample of chiral mixture to induce the chirality-dependent difference in the evolution of the two enantiomers. The frequencies of these fields are designed to be resonant with the corresponding electric-dipole transitions [21,22]. In the interaction picture with respect to $H_0^\alpha = \sum_j \omega_j |e_j^\alpha\rangle\langle e_j^\alpha| (\hbar = 1, j = 1, 2, 3)$, the Hamiltonian is given as

$$V_I^\alpha = \Omega_{21}^\alpha |e_2^\alpha\rangle\langle e_1^\alpha| + \Omega_{31}^\alpha |e_3^\alpha\rangle\langle e_1^\alpha| + \Omega_{32}^\alpha |e_3^\alpha\rangle\langle e_2^\alpha| + \text{H.c.}, \quad (1)$$

where ω_j are the energies of states $|e_j^\alpha\rangle$ with the ground state energy $\omega_0 = 0$ (the lower index 0 corresponds to ground state hereafter), and Ω_{jl}^α are the Rabi frequencies corresponding to the transition $|e_j^\alpha\rangle \leftrightarrow |e_l^\alpha\rangle$. The rotation-wave approximation has already been applied above. The difference between left-handed and right-handed chiral molecules is depicted by the Rabi frequencies [21,26,27] as $\Omega_{21}^L = \Omega_{21}^R = \Omega_{21}$, $\Omega_{31}^L = \Omega_{31}^R = \Omega_{31}$, and $\Omega_{32}^L = -\Omega_{32}^R = \Omega_{32}$.

The chirality dependence is reflected by the eigenvector $|d_j^\alpha\rangle = \sum_i n_{ij}^\alpha |e_i^\alpha\rangle (i, j = 1, 2, 3)$ of the cyclic three-level subsystem [21] under the Hamiltonian V_I^α, which satisfies

$V_I^\alpha |d_j^\alpha\rangle = E_j^\alpha |d_j^\alpha\rangle$ with E_j^α being the corresponding eigenvalues. Here, n_{ij}^α are the transformation matrix elements. Detailed derivations are presented in Supplemental Material [41]. Our method is designed to determine the signal from different enantiomers by distinguishing the frequencies E_j^α.

Three laser pulses (e.g., infrared pulses) in the BOXCARS geometry [36–40] with intervals τ and T are applied to probe the sample response. $\vec{k}_p$ ($p = a, b, c$) are the wave vectors and δt_p are the pulse durations. The central frequencies ν of the three pulses are set the same and resonant with the transition $|g^\alpha\rangle \leftrightarrow |e_1^\alpha\rangle$, i.e., $\nu = \omega_1$. The Hamiltonian describing the current system during a pulse interaction is written in the interaction picture as

$$V_p^\alpha(s) = \Omega_p(s) e^{i\vec{k}_p \cdot \vec{r}} |e_1^\alpha\rangle\langle g^\alpha| + \text{H.c.}, \quad (2)$$

where $\vec{r}$ is the spatial location of the molecule, $\Omega_p(s)$ is the Rabi frequency corresponding to the transition $|g^\alpha\rangle \leftrightarrow |e_1^\alpha\rangle$, and s is the time variable. Within the short durations of the probe pulses, we have neglected the interaction Hamiltonian V_I^α in Eq. (2) noticing that the incident pulses are strong and short enough that the interaction with the three driving fields becomes negligible, i.e., $\int_0^{\delta t_p} \Omega_{jl} ds \ll \int_0^{\delta t_p} \Omega_p(s) ds$.

In general, including only the transition $|g^\alpha\rangle \leftrightarrow |e_1^\alpha\rangle$ in Eq. (2) is reasonable when the bandwidths $\delta\nu$ of the incident pulses are much smaller than the frequency differences between the upper levels, i.e., $\delta\nu \ll \{\omega_{21}, \omega_{31}\}$ where $\omega_{ij} = |\omega_i - \omega_j|$. Another situation for the validity of Eq. (2) is when the transitions $|g^\alpha\rangle \leftrightarrow |e_2^\alpha\rangle$ and $|g^\alpha\rangle \leftrightarrow |e_3^\alpha\rangle$ are forbidden by the selection rules of electric dipole of chiral molecules [25,26,32]. In our discussion, the molecular levels are selected to fulfill such selection rules.

As shown by the pulse sequence in Fig. 1(b), the sample of chiral mixture interacts with the first pulse $\vec{k}_a$ and then interacts with the second pulse $\vec{k}_b$ after an evolution time τ. Later, after a second evolution time T, the sample interacts with the third pulse $\vec{k}_c$, while the signal emitted by the sample will be measured after a third evolution time t. After the whole process, the final wave function of the system is given (in the Schrödinger picture) as

$$|\psi^\alpha(\tau, T, t)\rangle = U_S^\alpha(t) U_{c,S}^\alpha U_S^\alpha(T) U_{b,S}^\alpha U_S^\alpha(\tau) U_{a,S}^\alpha |\psi_0^\alpha\rangle, \quad (3)$$

where the initial state $|\psi_0^\alpha\rangle$ is taken as the ground state $|g^\alpha\rangle$ under the typical low-temperature condition [17]. Here, $U_{p,S}^\alpha \equiv \exp[-iH_0^\alpha \delta t_p] U_p^\alpha(\delta t_p)$ and $U_S^\alpha(s) \equiv \exp[-iH_0^\alpha s] \exp[-iV_I^\alpha s]$ are the evolution operators with and without the probe pulses, respectively. The evolution operator $U_p^\alpha(\delta t_p) \equiv \mathcal{T} \exp[-i \int_0^{\delta t_p} V_p^\alpha(s) ds]$ (with $\mathcal{T}$ being the time-ordering operator) is simplified under the square pulse approximation [42] as $U_p^\alpha(\delta t_p) = \exp[-iV_p^\alpha \delta t_p]$.

Here, $V_p^\alpha = \Omega_p \exp[i\vec{k}_p \cdot \vec{r}]|e_1^\alpha\rangle\langle g^\alpha| + \text{H.c.}$ is the interaction Hamiltonian during square pulse $\vec{k}_p$ and Ω_p is the corresponding (time-independent) Rabi frequency.

The emission of the enantiomers is induced by the polarization $\boldsymbol{P}^\alpha(\tau, T, t) = \text{Tr}[\rho^\alpha(\tau, T, t)\boldsymbol{\mu}^\alpha]$, where $\rho^\alpha(\tau, T, t) \equiv |\psi^\alpha(\tau, T, t)\rangle\langle\psi^\alpha(\tau, T, t)|$ is the density matrix and $\boldsymbol{\mu}^\alpha$ is the electric-dipole operator. We particularly sort out the signal with the frequencies near ω_1, which is proportional to $\boldsymbol{P}_{10}^\alpha(\tau, T, t) \equiv \rho_{10}^\alpha(\tau, T, t)\boldsymbol{\mu}_{01} + \text{c.c.}$ (with $\boldsymbol{\mu}_{01}^\alpha = \boldsymbol{\mu}_{01}$ being the electric-dipole moment corresponding to the transition $|e_1^\alpha\rangle \to |g^\alpha\rangle$). Such sortation is accessible for the molecules in the gaseous phase where the linewidths of these levels are rather smaller than their energy spacings [24,43]. Moreover, by the phase matching, we select the *rephasing* (RP) signal emitted along the direction $\vec{k}_s = -\vec{k}_a + \vec{k}_b + \vec{k}_c$ as $\boldsymbol{P}_{10}^{\alpha,\text{RP}}(\tau, T, t) \exp[i\vec{k}_s \cdot \vec{r}]$, where

$$
\begin{aligned}
\boldsymbol{P}_{10}^{\alpha,\text{RP}}(\tau, T, t) = \boldsymbol{\mu}_{01} \sum_{l,l'=1}^{3} |n_{1l}^\alpha|^2 |n_{1l'}^\alpha|^2 \\
\times [\mathcal{A} e^{i(\omega_1 + E_l^\alpha)(\tau+T)} e^{-i(\omega_1 + E_{l'}^\alpha)(T+t)} \\
+ \mathcal{B} e^{i(\omega_1 + E_l^\alpha)\tau} e^{-i(\omega_1 + E_{l'}^\alpha)t}].
\end{aligned} \tag{4}
$$

Here, $\mathcal{A} = \mathcal{N}_a^2 \mathcal{N}_b^2 \mathcal{N}_c \beta_a^* \beta_b \beta_c^*$, $\mathcal{B} = \mathcal{N}_a^2 \mathcal{N}_b \mathcal{N}_c^2 \beta_a^* \beta_b^* \beta_c$, $\beta_p \simeq -i\Omega_p \delta t_p$ under the condition $\Omega_p \delta t_p \ll 1$ and $\mathcal{N}_p = (1 + |\beta_p|^2)^{-1/2}$ are the renormalized constants.

The two terms in Eq. (4) correspond to two different processes: the stimulated emission (SE) and the ground state bleach (GSB), illustrated by the double-side Feynman diagrams in Fig. 2. The two processes differ from each other at the duration time T, i.e., in the SE process the excited-state population is generated while in the GSB process the ground-state population is generated. By taking into account the relaxation rate Γ and the pure dephasing rate γ of the excited states (assumed to be the same for three excited states) in these processes, the *rephasing* signal in Eq. (4) is thus corrected as
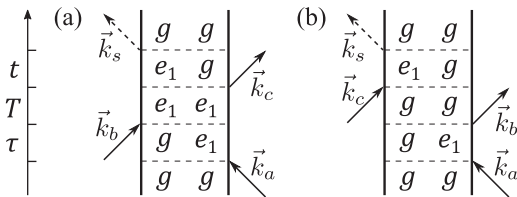

FIG. 2.   Double-side Feynman diagrams for (a) stimulated emission process and (b) ground state bleach process with the evolution times denoted on the left side. The solid and dashed arrows represent the incident probe pulses and the signals, respectively. In panel (a), the population for the first-excited state is generated after the first two pulses, while in panel (b), the ground-state population is generated.

$$
\begin{aligned}
\boldsymbol{P}_{10}^{\alpha,\text{RP}}(\tau, T, t) = \boldsymbol{\mu}_{01} \sum_{l,l'=1}^{3} |n_{1l}^\alpha|^2 |n_{1l'}^\alpha|^2 \\
\times [\mathcal{A} e^{i(\omega_1 + E_l^\alpha)(\tau+T)} e^{-i(\omega_1 + E_{l'}^\alpha)(T+t)} e^{-\Gamma'(\tau+t)} e^{-\Gamma T} \\
+ \mathcal{B} e^{i(\omega_1 + E_l^\alpha)\tau} e^{-i(\omega_1 + E_{l'}^\alpha)t} e^{-\Gamma'(\tau+t)}],
\end{aligned} \tag{5}
$$

where $\Gamma' \equiv (\Gamma/2) + \gamma$ indicates the decay of ρ_{10}.

For a mixture with N_L left-handed molecules and N_R right-handed molecules, the average *rephasing* signal is

$$
\boldsymbol{P}_{10}^{m,\text{RP}}(\tau, T, t) = \frac{N_L \boldsymbol{P}_{10}^{L,\text{RP}}(\tau, T, t) + N_R \boldsymbol{P}_{10}^{R,\text{RP}}(\tau, T, t)}{N_L + N_R}, \tag{6}
$$

where the upper index m means chiral mixture.

2D spectrum.—The measured signal in time domain is analyzed [39] with the 2D Fourier transform with respect to τ and t as

$$
\tilde{\boldsymbol{P}}_{10}^{m,\text{RP}}(\omega_\tau, T, \omega_t) \equiv \mathcal{F}[\boldsymbol{P}_{10}^{m,\text{RP}}(\tau, T, t)]. \tag{7}
$$

Substituting Eqs. (5) and (6) into Eq. (7), we find that each enantiomer will generate nine peaks at positions $(\omega_\tau, \omega_t) = (\omega_1 + E_l^\alpha, -\omega_1 - E_{l'}^\alpha)$ in the 2D spectrum with their magnitudes dominated by $|n_{1l}^\alpha|^2 |n_{1l'}^\alpha|^2$. The chirality dependence of E_j^α and n_{1j}^α is thus reflected by the spectrum.

We demonstrate our method on determining enantiomeric excess by an example of 1,2-propanediol with equal Rabi frequencies $\Omega_{21} = \Omega_{31} = \Omega_{32} = \Omega$ [9]. Thus, the eigenvalues of the Hamiltonians V_I^L and V_I^R are $E_1^L = 2\Omega = -E_1^R$, $E_2^L = E_3^L = -\Omega = -E_2^R = -E_3^R$. The transformation matrix elements involved in Eq. (5) are specified as $|n_{11}^\alpha|^2 = 1/3$ and $|n_{12}^\alpha|^2 + |n_{13}^\alpha|^2 = 2/3$.

For the numerical simulation, we choose the working states as $|g\rangle = |v_g\rangle|0_{0,0,0}\rangle$, $|e_1\rangle = |v_e\rangle|1_{1,1,1}\rangle$, $|e_2\rangle = |v_e\rangle|2_{2,1,2}\rangle$, and $|e_3\rangle = |v_e\rangle|2_{2,0,1}\rangle$, where the chirality index is neglected. The ket vector $|v_g\rangle$ ($|v_e\rangle$) denotes the corresponding vibrational ground (first-excited) state and $|J_{K_a,K_c,M}\rangle$ denotes the rotational state [44]. Under such a working state arrangement, only the transition $|g\rangle \leftrightarrow |e_1\rangle$ is induced by the pulses, and the others are forbidden due to the selection rules [25,26,32]. The transition frequencies are given as $\omega_{10}/2\pi \simeq 4.33$ THz, $\omega_{21}/2\pi \simeq 29.21$ GHz, $\omega_{31}/2\pi \simeq 29.31$ GHz, and $\omega_{32}/2\pi \simeq 100.76$ MHz [22,44–46]. We take the Rabi frequency $\Omega/2\pi \simeq 2$ MHz, the relaxation rate $\Gamma/2\pi \simeq 1$ kHz, and the pure dephasing rate $\gamma/2\pi \simeq 0.1$ MHz according to the recent experiments [24,43]. The value of the Rabi frequency Ω is achievable with the microwave field in the existing experimental setups [17,24]. We assume that all the probe pulses are the same except for their direction by taking $\Omega_p/2\pi \simeq 50$ MHz and $\delta t_p \simeq 0.5$ ns, with the bandwidth $\delta\nu \simeq 2\pi \times 1.8$ GHz $\ll \{\omega_{21}, \omega_{31}\}$ [47].
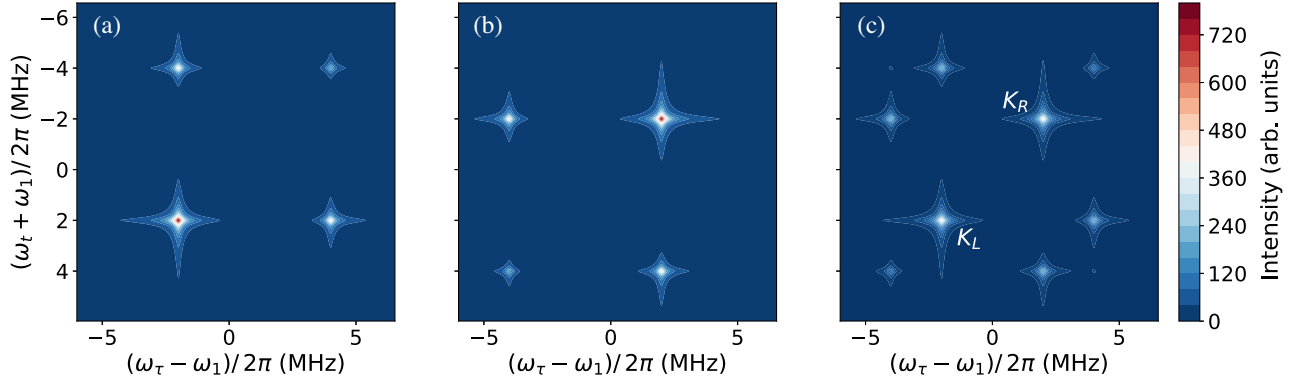
FIG. 3. 2D spectra (in arbitrary units, arb. units) of (a) pure left-handed chiral molecules, (b) pure right-handed chiral molecules, and (c) racemic mixture with equal left-handed and right-handed chiral molecules. These spectra are obtained via 2D fast Fourier transform and only the absolute values of the transform result are taken. The time-domain signals are scanned from 0 to 0.2 ms with 0.02 μs time step for both τ and t, while T is set to be zero here.

The pulse frequency $\nu = \omega_{10}$ in our example falls in the region of terahertz (THz) spectroscopy. For the 2D-THz measurement, the BOXCARS geometry is hard to be implemented due to the large diameter of terahertz beams [48]. Instead, the collinear geometry [49,50] is used along with additional detection methods, such as electrooptic sampling and chopping detection [48–50], to sort out the desired *rephasing* signal.

The numerical results are shown in Fig. 3 where the time-domain signals are detected every 0.02 μs with the scale 0.2 ms for time coordinates τ and t. The 2D spectra are obtained via 2D fast Fourier transform by taking the absolute values of the transform result. To obtain a maximum response, we have taken $T = 0$ in Fig. 3, since the signal should decay with relaxation rate Γ during the evolution time T, as indicated by Eq. (5).

Because of the degeneracy for the eigenvalues E_j^α in our example, nine peaks reduce to four (two diagonal and two off-diagonal peaks) for each enantiomer in Figs. 3(a) and 3(b). For a chiral mixture, eight peaks are naturally divided into two groups with the help of off-diagonal peaks. The two groups are associated with specific enantiomers by detecting any sample containing one dominant enantiomer since the dominator generates higher peaks. Hence, a standard enantiopure sample is not needed in our method.

To determine the enantiomeric excess, we denote K_L (K_R) the amplitude of the highest peak corresponding to the degenerate levels $|d_2^L\rangle$ and $|d_3^L\rangle$ ($|d_2^R\rangle$ and $|d_3^R\rangle$) for left-handed (right-handed) chiral molecules [e.g., see Fig. 3(c) in the case of racemic mixture with $N_L = N_R$],

$$
\begin{aligned}
K_{L/R} &= (N_L + N_R) \times |\tilde{\boldsymbol{P}}_{10}^{m,\mathrm{RP}}(\omega_\mp, T, -\omega_\mp)|, \\
&= N_L |\tilde{\boldsymbol{P}}_{10}^{L,\mathrm{RP}}(\omega_\mp, T, -\omega_\mp)| + N_R |\tilde{\boldsymbol{P}}_{10}^{R,\mathrm{RP}}(\omega_\mp, T, -\omega_\mp)|
\end{aligned}
\tag{8}
$$

(the indices "$-$" and "$+$" on the right-hand side correspond to indices L and R on the left-hand side, respectively), where $\omega_\mp = \omega_1 \mp \Omega$. In the strong coupling condition $\{\Gamma, \gamma\} \ll \Omega$, the peaks are well separated, and K_L (K_R) is approximately linearly proportional to N_L (N_R),

$$
K_{L/R} \simeq N_{L/R} |\tilde{\boldsymbol{P}}_{10}^{L/R,\mathrm{RP}}(\omega_\mp, T, -\omega_\mp)|.
\tag{9}
$$

Noticing the equal coefficients $|n_{12}^\alpha|^2 + |n_{13}^\alpha|^2 = 2/3$ in Eq. (5) in the degenerate case, the signal intensities for left-handed and right-handed chiral molecules are the same, i.e., $|\tilde{\boldsymbol{P}}_{10}^{L,\mathrm{RP}}(\omega_-, T, -\omega_-)| = |\tilde{\boldsymbol{P}}_{10}^{R,\mathrm{RP}}(\omega_+, T, -\omega_+)|$. Thus, our estimation of the enantiomeric excess is

$$
\varepsilon_e = \frac{K_L - K_R}{K_L + K_R},
\tag{10}
$$

and the error of our estimation is $\delta = \varepsilon_e - \varepsilon$ with the real enantiomeric excess $\varepsilon = (N_L - N_R)/(N_L + N_R)$. Figure 4 shows the effectiveness of our estimation by numerically giving the absolute errors for various Rabi frequencies Ω. In most regions, the absolute errors of our estimation are smaller than 2×10^{-3}.

Our estimation is not limited to the degenerate case with the arrangement $\Omega_{21} = \Omega_{31} = \Omega_{32} = \Omega$. When Ω_{21}, Ω_{31}, and Ω_{32} are not equal, one can still denote K_L (K_R) the amplitude of the highest peak for left-handed (right-handed) molecules with $K_\alpha \simeq N_\alpha |\tilde{\boldsymbol{P}}_{10}^{\alpha,\mathrm{RP}}(\omega_\alpha, T, -\omega_\alpha)|$. $\omega_\alpha = \omega_1 + E_\xi^\alpha$ (with $E_\xi^L = -E_\xi^R$) are used to replace $\omega_\mp$ in Eq. (9). The signal intensities in Eq. (5) for the left-handed and right-handed molecules have the relation $|\tilde{\boldsymbol{P}}_{10}^{L,\mathrm{RP}}(\omega_L, T, -\omega_L)|/|n_{1\xi}^L|^4 = |\tilde{\boldsymbol{P}}_{10}^{R,\mathrm{RP}}(\omega_R, T, -\omega_R)|/|n_{1\xi}^R|^4$. We prove a general relation $|n_{1\xi}^L|^2 = |n_{1\xi}^R|^2$ with details in Supplemental Material [41]. Therefore, the estimation of the enantiomeric excess is still $\varepsilon_e = (K_L - K_R)/(K_L + K_R)$.
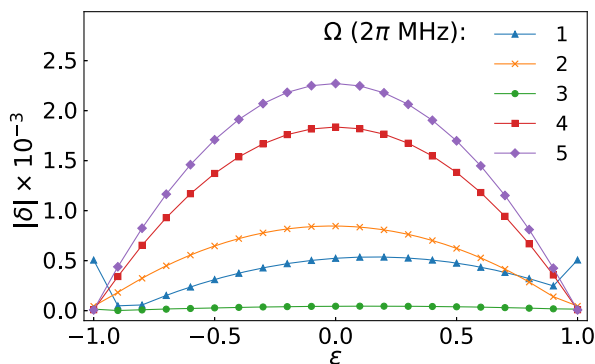
FIG. 4. The absolute errors of our estimation on the enantiomeric excess for different Rabi frequencies. The other parameters and scanned path are adopted from Fig. 3.

To implement measurement with broadband probe pulses, additional levels (other than $|e_2\rangle$ and $|e_3\rangle$) may be included in the spectra if one cannot selectively induce $|e_1\rangle \leftrightarrow |g\rangle$ transition. In such a case, we can apply the chopping methods [48–50] where two signals ($\tilde{P}_{10,\text{on}}^{m,\text{RP}}$ and $\tilde{P}_{10,\text{off}}^{m,\text{RP}}$) are measured with the microwaves on and off. The subtraction $\tilde{P}_{10,\text{on}}^{m,\text{RP}} - \tilde{P}_{10,\text{off}}^{m,\text{RP}}$ will remove any contributions from the additional levels, since their peak locations and intensities are not affected by the microwave modulations.

Conclusion.—We have proposed a new method on enantiomeric excess determination via the 2D spectroscopy based on the generic four-level structure of chiral molecules in the gaseous phase. The procedure of the current method is summarized with two operations, *modulation* and *probe*. The three constant driving fields *modulate* the system and cause the different frequency shifts of the upper three levels for the two enantiomers. The signal generated by the four-wave-mixing process is *probed* via the 2D spectrum, where the peaks reflect the chirality dependence. With the off-diagonal peaks, the corresponding chirality of the peaks can be identified with any sample containing one dominant enantiomer. In the strong coupling condition $\{\Gamma, \gamma\} \ll \Omega$, the peak amplitudes are approximately linear with the quantities of the corresponding chiral molecules. Hence, the enantiomeric excess is estimated by comparing the peak intensities.

The advantages of the current method lie in two aspects. First, the tunable driving fields allow the creation of significant difference between enantiomers, comparing with the traditional enantiodetection methods with the weak magnetic-dipole or electric-quadrupole interactions. Second, the application of 2D spectroscopy allows the separate contributions of the enantiomers within one single spectrum, without the need for standard enantiopure sample, benefited from the inherit resolution of 2D spectroscopy.

*hdong@gscaep.ac.cn
†yongli@hainanu.edu.cn

[1] P. G. Mezey, *New Developments in Molecular Chirality,* Understanding Chemical Reactivity (Springer, Netherlands, 1991).
[2] M. Quack, Angew. Chem., Int. Ed. Engl. **28,** 571 (1989).
[3] A. Eilam and M. Shapiro, Phys. Rev. Lett. **110,** 213004 (2013).
[4] K. K. Lehmann, J. Chem. Phys. **149,** 094201 (2018).
[5] F. Suzuki, T. Momose, and S. Y. Buhmann, Phys. Rev. A **99,** 012513 (2019).
[6] M. Shapiro, E. Frishman, and P. Brumer, Phys. Rev. Lett. **84,** 1669 (2000).
[7] P. Brumer, E. Frishman, and M. Shapiro, Phys. Rev. A **65,** 015401 (2001).
[8] D. Gerbasi, M. Shapiro, and P. Brumer, J. Chem. Phys. **115,** 5349 (2001).
[9] P. Král, I. Thanopulos, M. Shapiro, and D. Cohen, Phys. Rev. Lett. **90,** 033001 (2003).
[10] E. Frishman, M. Shapiro, and P. Brumer, J. Phys. B **37,** 2811 (2004).
[11] C. Ye, Y.-Y. Chen, Q. Zhang, and Y. Li, J. Phys. B **54,** 145102 (2021).
[12] A. Ghosh and P. Fischer, Phys. Rev. Lett. **97,** 173002 (2006).
[13] P. J. Stephens, J. Phys. Chem. **89,** 748 (1985).
[14] Y. He, W. Bo, R. K. Dukor, and L. A. Nafie, Appl. Spectrosc. **65,** 699 (2011).
[15] T. K. Begzjav, Z. Zhang, M. O. Scully, and G. S. Agarwal, Opt. Express **27,** 13965 (2019).
[16] W. Z. Jia and L. F. Wei, Phys. Rev. A **84,** 053849 (2011).
[17] D. Patterson, M. Schnell, and J. M. Doyle, Nature (London) **497,** 475 (2013).
[18] D. Patterson and J. M. Doyle, Phys. Rev. Lett. **111,** 023008 (2013).
[19] V. A. Shubert, D. Schmitz, C. Pérez, C. Medcraft, A. Krin, S. R. Domingos, D. Patterson, and M. Schnell, J. Phys. Chem. Lett. **7,** 341 (2016).
[20] S. Lobsiger, C. Perez, L. Evangelisti, K. K. Lehmann, and B. H. Pate, J. Phys. Chem. Lett. **6,** 196 (2015).
[21] C. Ye, Q. Zhang, Y.-Y. Chen, and Y. Li, Phys. Rev. A **100,** 033411 (2019).
[22] Y.-Y. Chen, C. Ye, Q. Zhang, and Y. Li, J. Chem. Phys. **152,** 204305 (2020).
[23] C. Ye, Y. Sun, and X. Zhang, J. Phys. Chem. Lett. **12,** 8591 (2021).
[24] S. Eibenberger, J. Doyle, and D. Patterson, Phys. Rev. Lett. **118,** 123002 (2017).
[25] C. Ye, Q. Zhang, and Y. Li, Phys. Rev. A **98,** 063401 (2018).
[26] A. Jacob and K. Hornberger, J. Chem. Phys. **137,** 044313 (2012).
[27] P. Král and M. Shapiro, Phys. Rev. Lett. **87,** 183002 (2001).
[28] Y. Li and C. Bruder, Phys. Rev. A **77,** 015403 (2008).
[29] W. Z. Jia and L. F. Wei, J. Phys. B **43,** 185402 (2010).

[30] C. Pérez, A. L. Steber, S. R. Domingos, A. Krin, D. Schmitz, and M. Schnell, Angew. Chem., Int. Ed. Engl. **56,** 12512 (2017).

[31] N. V. Vitanov and M. Drewsen, Phys. Rev. Lett. **122,** 173202 (2019).

[32] M. Leibscher, T. F. Giesen, and C. P. Koch, J. Chem. Phys. **151,** 014302 (2019).

[33] Y. Li, C. Bruder, and C. P. Sun, Phys. Rev. Lett. **99,** 130403 (2007).

[34] X. Li and M. Shapiro, J. Chem. Phys. **132,** 194315 (2010).

[35] B. Liu, C. Ye, C. P. Sun, and Y. Li, Phys. Rev. A **104,** 013113 (2021).

[36] S. Mukamel, *Principles of Nonlinear Optical Spectroscopy*, Oxford Series in Optical and Imaging Sciences (Oxford University Press, New York, 1995).

[37] M. Cho, *Two-Dimensional Optical Spectroscopy* (CRC Press, Boca Raton, 2009).

[38] S.-H. Shim and M. T. Zanni, Phys. Chem. Chem. Phys. **11,** 748 (2009).

[39] G. S. Schlau-Cohen, A. Ishizaki, and G. R. Fleming, Chem. Phys. **386,** 1 (2011).

[40] C. T. Middleton, A. M. Woys, S. S. Mukherjee, and M. T. Zanni, Methods **52,** 12 (2010).

[41] See Supplemental Material at http://link.aps.org/supplemental/10.1103/PhysRevLett.129.103201 for the detailed derivations.

[42] J.-F. Chen, H. Dong, and C.-P. Sun, Phys. Scr. **94,** 105508 (2019).

[43] D. Patterson and J. M. Doyle, Mol. Phys. **110,** 1757 (2012).

[44] R. N. Zare, *Angular Momentum: Understanding Spatial Aspects in Chemistry and Physics* (John Wiley, New York, 1988).

[45] B. E. Arenas, S. Gruet, A. L. Steber, and M. Schnell, J. Mol. Spectrosc. **337,** 9 (2017).

[46] F. Lovas, D. Plusquellic, B. H. Pate, J. L. Neill, M. T. Muckle, and A. J. Remijan, J. Mol. Spectrosc. **257,** 82 (2009).

[47] J.-C. Diels and W. Rudolph, in *Ultrashort Laser Pulse Phenomena*, 2nd ed. (Academic Press, Burlington, 2006).

[48] M. Woerner, W. Kuehn, P. Bowlan, K. Reimann, and T. Elsaesser, New J. Phys. **15,** 025039 (2013).

[49] J. Lu, Y. Zhang, Y. Hwang Harold, K. Ofori-Okai Benjamin, S. Fleischer, and A. Nelson Keith, Proc. Natl. Acad. Sci. U.S.A. **113,** 11800 (2016).

[50] K. Reimann, M. Woerner, and T. Elsaesser, J. Chem. Phys. **154,** 120901 (2021).